Taking Snapshots of Photosynthetic Water Oxidation Using Femtosecond X-ray Diffraction and Spectroscopy

Jan Kern[1,2], **Rosalie Tran**[1], **Roberto Alonso-Mori**[2], **Sergey Koroidov**[3], **Nathaniel Echols**[1], **Johan Hattne**[1], **Mohamed Ibrahim**[4,5], **Sheraz Gul**[1], **Hartawan Laksmono**[6], **Raymond G. Sierra**[6], **Richard J. Gildea**[1,†], **Guangye Han**[1], **Julia Hellmich**[4,5], **Benedikt Lassalle-Kaiser**[1,‡], **Ruchira Chatterjee**[1], **Aaron S. Brewster**[1], **Claudiu A. Stan**[6], **Carina Glöckner**[5], **Alyssa Lampe**[1], **Dörte DiFiore**[5], **Despina Milathianaki**[2], **Alan R. Fry**[2], **M. Marvin Seibert**[2,¶], **Jason E. Koglin**[2], **Erik Gallo**[7], **Jens Uhlig**[7], **Dimosthenis Sokaras**[8], **Tsu-Chien Weng**[8], **Petrus H. Zwart**[1], **David E. Skinner**[9], **Michael J. Bogan**[2,6], **Marc Messerschmidt**[2], **Pieter Glatzel**[7], **Garth J. Williams**[2], **Sébastien Boutet**[2], **Paul D. Adams**[1], **Athina Zouni**[4,5], **Johannes Messinger**[3], **Nicholas K. Sauter**[1], **Uwe Bergmann**[2,*], **Junko Yano**[1,*], and **Vittal K. Yachandra**[1,*]

[1]Physical Biosciences Division, Lawrence Berkeley National Laboratory, Berkeley, CA 94720, USA

[2]LCLS, SLAC National Accelerator Laboratory, Menlo Park, CA 94025, USA

[3]Institutionen för Kemi, Kemiskt Biologiskt Centrum, Umeå Universitet, Umeå, Sweden

[4]Institut für Biologie, Humboldt-Universität zu Berlin, D-10099 Berlin, Germany

[5]Max-Volmer-Laboratorium für Biophysikalische Chemie, Technische Universität, D-10623 Berlin, Germany

[6]PULSE Institute, SLAC National Accelerator Laboratory, Menlo Park, CA 94025, USA

[7]European Synchrotron Radiation Facility, F-38043 Grenoble Cedex, France

*Corresponding authors. bergmann@slac.stanford.edu (U.B.), jyano@lbl.gov, (J.Y.), vkyachandra@lbl.gov (V.K.Y.).
†Present address: Diamond Light Source, Harwell Science and Innovation Campus, Didcot, Oxfordshire OX11 0DE, UK
‡Present address: Synchrotron SOLEIL, F-91192 Gif-Sur-Yvette, France
¶Present address: Department of Cell and Molecular Biology, Uppsala Universitet, 751 24 Uppsala, Sweden

[8]SSRL, SLAC National Accelerator Laboratory, Menlo Park, CA 94025, USA

[9]National Energy Research Scientific Computing Center, Lawrence Berkeley National Laboratory, Berkeley, CA 94720, USA

Abstract

The dioxygen we breathe is formed from water by its light-induced oxidation in photosystem II. O_2 formation takes place at a catalytic manganese cluster within milliseconds after the photosystem II reaction center is excited by three single-turnover flashes. Here we present combined X-ray emission spectra and diffraction data of 2 flash (2F) and 3 flash (3F) photosystem II samples, and of a transient 3F′ state (250 µs after the third flash), collected under functional conditions using an X-ray free electron laser. The spectra show that the initial O-O bond formation, coupled to Mn-reduction, does not yet occur within 250 µs after the third flash. Diffraction data of all states studied exhibit an anomalous scattering signal from Mn but show no significant structural changes at the present resolution of 4.5 Å. This study represents the initial frames in a molecular movie of the structural changes during the catalytic reaction in photosystem II.

Aerobic life on earth is supported by the constant regeneration of dioxygen through photosynthetic water oxidation in green plants, algae, and cyanobacteria. This reaction takes place in photosystem II (PS II), a multi-subunit membrane protein complex. PS II couples the one-electron photochemistry of the primary charge separation at the reaction center with the four-electron redox chemistry of water oxidation at the Mn_4O_5Ca cluster of the oxygen evolving complex (OEC) at the lumenal side of the protein complex, utilizing the spatial and temporal organization of the electron donor and acceptor cofactors in PS II[1,2]. This well-controlled electron and proton flow results in the high quantum efficiency of PS II.

During the water oxidation reaction, the OEC functions as a redox capacitor by storing four oxidizing equivalents before the release of molecular oxygen. Starting from the dark stable S_1 state, the oxidation state of the OEC is increased by one upon each light excitation of PS II until the highest oxidized stable intermediate state, S_3, is reached. Following the next light-excitation, the OEC is oxidized one more time to form the transient $S_3Y_Z{}^{ox}$ and S_4 states that lead to dioxygen formation, which converts the OEC to its most reduced state, S_0[3]. The fourth light-excitation sets the OEC back to the S_1 state, and thereby completes the cycle (Fig. 1A).

Much structural and mechanistic information about PS II, the OEC and the O-O bond formation was gained through mass spectrometric[4], various spectroscopic[4–9], crystallographic[10–13] and theoretical[14–16] studies over the past decade. In particular, the most recent structure, inferred from X-ray diffraction (XRD) data, has provided detailed geometric information of the OEC, including ligands and bound water molecules[13]. Most of the experimental studies, however, are carried out at cryogenic temperatures and represent a static picture of the system in a frozen state. While the stable intermediate states, S_0 through S_3, can be trapped and studied at cryogenic temperatures, the critical $S_3 \rightarrow S_3Y_Z{}^{ox} \rightarrow S_4 \rightarrow S_0$ step – where dioxygen is formed, two protons and O_2 are released, and where at least one substrate water binds – only occurs under ambient conditions and has no intermediates that

can be cryo-trapped. To date there has been only one transient X-ray spectroscopy study of the $S_3 \rightarrow S_3Y_Z^{ox} \rightarrow S_4 \rightarrow S_0$ transition been performed at room temperature.[17] More detailed investigations of the transient states by X-ray spectroscopy and by kinetic crystallography have been hampered due to the severe radiation damage especially to the Mn_4CaO_5 cluster that is significantly faster at room temperature (RT) as compared to cryogenic conditions. However, X-ray-induced changes, particularly at the redox-active metal site, have even been an issue for experiments carried out at cryogenic temperatures[18–20].

We have recently introduced a combined spectroscopy and diffraction data collection methodology at RT[21] using the "probe before destroy" method[22–24] made possible by the ultra-short (fs) and bright X-ray pulses of an X-ray free electron laser (XFEL). In this approach, XRD data and Mn Kβ-X-ray emission spectra (XES), sensitive to the metal charge density[25,26], are measured simultaneously from micrometer-sized crystals of PS II, thereby obtaining information about the geometric and the electronic structure of the active site, under identical conditions. Due to the ultra-short fs X-ray pulse duration, the sample is probed before the manifestation of X-ray induced changes – which predominantly take place on the picosecond time scale (for damage to the atomic structure) – even under ambient conditions. One should note that with conventional synchrotron X-ray sources the main source of radiation damage is via the generation of radicals form the solvent (water). Subsequent diffusion of these radicals leads to specific damage (e.g. reduction of metal sites) and modification of amino acid side chains (e.g. decarboxylations). Such events are diffusion controlled and occur on a longer time scale (> picoseconds) and seem not to be dependent on the dose rate. Earlier work[21,27] showed that the approach of using ultrafast (<50 fs) and ultrabright (10^{12} photons/pulse) X-ray pulses permits the collection of XES and XRD data from intact PS II, and we reported results from the dark-adapted (S_1) and the one flash (S_2) samples with an XRD resolution limited to 5.5 Å.

Here, we present XES and XRD data from the last step of the Kok cycle, where O_2 is evolved, with an improved resolution of 4.5 Å. This step, triggered by the third flash given to dark-adapted PS II samples, advances the PS II complex from the S_3 to the S_0 state, via the transient $S_3Y_Z^{ox}$ and S_4 states ($S_3 \rightarrow S_3Y_Z^{ox} \rightarrow S_4 \rightarrow S_0$ transition). Furthermore, we observe an anomalous signal for the Mn atoms in the OEC from all the states, including the transient $S_3Y_Z^{ox}$ state. This observation supports the quality of our XRD data and also the data analysis protocols, and we envision that the Mn anomalous signal could be used as a sensitive probe for monitoring changes of the atomic positions of Mn in the OEC during the catalytic cycle in future studies at higher resolution.

Results

XES at Different Time Points in the Catalytic Cycle

PS II was advanced through its reaction cycle *in situ*, using a flow/illumination scheme (Fig. 1B) employing an electrospun liquid jet[28]. The protocol consisted of visible-laser illumination using three optical fibers directly attached to the sample delivery capillary, and an additional laser for illumination of the sample in the jet (see Methods). The temporal frequency for illumination was chosen to match the sample flow rate, so that each volume

segment was illuminated by each fiber once while passing through the capillary. The setup also allows enough time (~0.5 s) for complete PS II turnover between consecutive illuminations, which takes into account the slower acceptor side reactions[7,29–31], while being rapid enough to avoid significant decay of the S states, that are stable for on the order of several tenth of seconds. The fourth laser (labeled "laser 4" in Fig. 1B) illuminated the sample in the jet, to study transients during the S_3 to S_0 transition by changing the timing between the 3rd visible-laser pulse and the X-ray probe pulse.

O_2 detection via membrane-inlet mass spectrometry (MIMS) was used for optimizing the conditions for S-state turnover in the capillary flow sample delivery system, using a facsimile of the flow/illumination set up employed at LCLS (see Methods). One of the most important factors in the illumination scheme is the required light intensity for efficient turnover through the S_i state cycle. To low intensities can lead to only partial turnover of the samples, while too high intensities increase the miss parameter via light scattering along the capillary, and may also inactivate the sample. The optimal light intensity can be found by the quality of the O_2 oscillation pattern, and also by the total O_2 produced per PSII complex and flash number. The former method should normally be sufficient, but a small uncertainty remains if there can be a certain part of the sample that never sees any light, and thus does not contribute to the oscillation pattern. To address this question approach, the latter method needs to be employed (see Methods), which requires the absolute calibration of the MIMS signals. The amount of 0.73 O_2/RC after 3 flashes shows that the light conditions used for illumination are optimal for saturating all PSII reaction centers in the sample (Fig. 2A). The O_2 evolution patterns obtained from PS II solutions and PS II microcrystals (Fig. 2B) show light induced turnover of the catalytic cycle as expected. Analysis of the flash pattern indicates that the S_3 state is the majority component ($\geq 55\%$) in the samples given two visible-laser flashes (2F) with virtually no S_0 state present. In contrast, the largest component in the 3F samples is the S_0 state ($\geq 40\%$). Therefore the difference between the 3F and 2F samples is dominated by the formation of the S_0 state at the expense of the S_3 state.

We measured XES on PS II solutions at the CXI instrument[32] at LCLS (see Methods). As shown in Fig. 3, a clear shift between the 2F (S_3-enriched) and 3F (S_0-enriched) spectra is observable. Calculation of the first moment (see Methods) revealed that the 3F spectrum is shifted about 0.1 eV to higher energies indicating a reduction of Mn[26], as expected for the transition of the OEC from the highly oxidized S_3 to the most reduced S_0 state, in which the formal oxidation states are assigned as Mn_4^{IV} and $Mn_3^{III}Mn^{IV}$, respectively[1,2,6,33,34]. Comparing these data to synchrotron radiation (SR) data collected at cryogenic temperature from *T. elongatus* PS II and previously recorded data from spinach PS II[35] shows a very similar trend (Fig. 3C and Supplementary Fig. 1).

In addition to the 2F and 3F spectra, we measured the XES at a time point 250 μs (3F′) after the third flash using lasers 2, 3, and 4 (Fig. 1). The XES for this transient state is similar in position to the 2F spectrum (Fig. 3A,B), but its shape is different with broadening towards the lower energy side. While such broadening could be caused by oxidation of a fraction of the lower S-states (S_1 and S_2) in our sample, it could also be due to light-induced changes in the electronic structure of the S_3-fraction. Nevertheless, the result shows that there is no

significant reduction or oxidation of the Mn taking place within the 250 μs time span between the third visible-laser excitation pulse and the X-ray probe pulse.

X-ray Diffraction in the Higher S-states

XRD data from 2F (S_3-enriched), 3F (S_0-enriched), and 3F′ ($S_3Y_Z^{ox}$-enriched; 250 μs after the 3rd flash) PS II crystals as well as in the dark state (S_1) were collected. Microcrystals of PS II were prepared using a new seeding protocol (see Methods). Clear Bragg spots were observed to a resolution of ~4.1 Å, with thermal diffuse scattering extending well beyond this to ~3.0 Å, indicative of correlated atomic motion in the crystal. For the 2F data, a total of 16,973 indexed patterns were merged resulting in a data set of 4.5 Å resolution (see Table 1, Supplementary Tables 1 and 2 for details). The resolution cutoff for the merged data sets was chosen based on the resolution-dependence both of the multiplicity and of $CC_{1/2}$, the correlation coefficient of semi-datasets merged from odd- and even-numbered images[36]; i.e. completeness > 90%, multiplicity > 6, and $CC_{1/2} > 30\%$. Likewise, data sets of 3F, 3F′ and 0F states were obtained with resolutions of 4.6 Å (13,094 lattices), 5.2 Å (7,850 lattices) and 4.9 Å (6,695 lattices), respectively (Table 1, Supplementary Tables 1, 3–5). Electron density maps for all four states are shown in Fig. 4, Supplementary Figs. 2 and 3. A comparison with the SR data cut to the same resolution shows that the level of detail visible is as expected for this resolution range (Supplementary Fig. 4). The occupancy for selected non-protein molecules was set to zero and the simulated annealing omit maps were computed for all data sets, to remove potential model bias arising from phasing with a complete, high-resolution starting model (pdb: 3bz1)[12.] The result clearly shows the electron density of the Mn_4O_5Ca cluster, the non-heme Fe, the chlorophyll and even partially for the quinone cofactors (Supplementary Fig. 3) in the $mF_o–DF_c$ difference maps. The regions around the OEC, the acceptor-side quinones, and non-heme iron, where the largest changes are expected, were inspected for changes between the different states. No statistically significant changes were observed in the $2mF_o–DF_c$ maps of the individual data sets (Fig. 4A,B, Supplementary Fig. 2 and 3) and in the isomorphous difference maps (mF_o-mF_o) between the different data sets (Fig. 4C, D, Supplementary Fig. 5). This shows that any structural changes related to the S-state transitions are smaller than what we can detect at the current resolution. However, it should be noted that the mF_o-DF_c Fourier maps contain several features that are observed consistently in both monomers and all flash states; namely an electron density peak at the position of the OEC when viewed at a contour level of +3σ, a small peak 10 Å distant that appears to be coordinated by residues Glu 333 and Asp 61 of the D1 polypeptide, and other nearby peaks. Smaller negative peaks are seen at the −3σ contour, for example close to Val 185 and Phe 182 of the D1 protein (Supplementary Fig. 6). We observe these low intensity peaks at the same positions generally in both monomers and across all four illuminated states. This suggests that they are not artifacts of the Fourier transform, and are rather due to structural differences between SR data collected at cryogenic temperature and the room temperature data presented here. However, the current resolution does not allow them to be fully modeled in our final atomic coordinate sets.

Measurement of Anomalous XRD Signal from Mn in PS II

Accurate determination of the Bragg spot intensities and the derived structure factors is challenging for single-shot crystallography at XFELs[21,23,24]. As a control to validate the

data quality and our analysis protocol, we investigated whether small anomalous differences could be detected in the recorded Bragg spot intensities. Such differences between inversion-related Bragg spots (Bijvoet pairs) arise from the collection of diffraction data at energies above an absorption edge and are often only in the order of ~1% of the total signal intensity. We used an incident energy of 7.1 keV in our current XES/XRD data collection, which is close to the Mn edge (6.54 keV), and favors observing the anomalous signal from Mn in the OEC.

As a positive control of the methodology, we first analyzed microcrystal diffraction data from a model system, thermolysin, which natively binds one Zn and several Ca ions[37]. Data from thermolysin microcrystals were collected at 1.27 Å (9.76 keV), about 100 eV above the Zn edge (9.66 keV). Diffraction was observed out to the corners of the detector (1.50 Å) and the integrated intensities were merged to obtain a dataset to 1.80 Å resolution (Table 1, Supplementary Table 6). Analysis of the Bijvoet pairs in the merged data showed a clear anomalous signal contribution, and anomalous difference maps showed a clear maximum, 18 σ above the mean, located at the position of the Zn ion as well as lower maxima for three of the four Ca ions and for the sulfur of one of the methionine residues (Figs. 5A, B and Supplementary Fig. 7).

In PS II, a clear anomalous signal (Fig. 5C, D, Fig. 6 and Supplementary Fig. 8 and 9) from Mn in the OEC is also detected in all four data sets (0F, 2F, 3F, and 3F′) (Table S1). Figs. 5C,D show the anomalous difference map from the 3F data after omitting the OEC and performing simulated annealing refinement. It is evident from the overview shown in Fig. 5C that the largest peak (σ > 6) in the anomalous density is located at the position of the OEC. The density covers the Mn ions in the cluster and does not include the Ca (Fig. 5D) as expected from the weaker anomalous contribution of Ca at 7.1 keV (f'' of 1.6 for Ca compared to 3.4 for Mn at 7.1 keV). Similar results were obtained for the other PS II datasets for both monomers in the PS II dimer (Fig. 6 and Supplementary Fig. 8 and 9). It should ne noted however that the anomalous difference Patterson maps did not reveal peaks above the noise level attributable to Mn. This result is expected as also the anomalous data measured at SR sources at 3.5 Å resolution[10] did not yield any peaks in the Patterson map above the noise level, due to the large protein mass and the low number of anomalous scatterers per unit cell volume.

Discussion

The quality of the PS II XRD data reported here for the S_1 state is improved compared to the previously obtained XFEL data: 4.5 Å vs 5.7 Å[21]. Due to the inherent fluctuations in pulse intensity, crystal size and crystal quality in single shot microcrystal experiments at an XFEL, the signal strength varies from shot to shot. Therefore, we expect a distribution of diffraction images with different maximum resolution. To avoid adding noise into the diffraction data, an individual resolution cutoff was computed for each diffraction image based on the signal strength (see Methods). The observed distribution of the resolution for PS II as well as for thermolysin explains why the multiplicity in both cases (Supplementary Tables 2–6) decreases steadily in the higher resolution shells.

Recently the first observation of an anomalous signal from femtosecond diffraction experiments with microcrystals at an XFEL[38] and the first successful de-novo phasing of lysozyme at 2.1 Å resolution using the anomalous signal of gadolinium obtained in an XFEL experiment were reported[39]. In the gadolinium phasing experiment of lysozyme the anomalous signal strength was around 5–15%[39]. In comparison we expect an anomalous signal of < 1% for Mn in PS II and of ~1.5% for Zn in thermolysin. The observation of the very strong anomalous peak for Zn in the thermolysin data indicates that the Bragg peak intensities were determined with sufficient accuracy to extract the weak anomalous difference (see ref. [40] for a report on determining the anomalous Zn signal of thermolysin from SR measurements). Furthermore, the presence of the anomalous density for Mn in all of the PS II data sets, despite the expected low signal strength, confirms the quality of the data, and implies that structure factors can be extracted reliably from the current PS II data sets. In this regard it should be noted that even the high-resolution shell of the data still contains a considerable amount of anomalous signal as can be seen in Supplementary Fig. 9B.

As described above, the electron density of PS II shows the level of detail expected at the specified resolutions (4.5–5.2 Å, depending on number of collected images per S-state; Supplementary Fig. 4). The quinone co-factors (Q_A in the dark, 2F and 3F data; Q_B in the 3F data), that were not visible in the previous XFEL data due to limited resolution, are now partially visible in the $mF_o–DF_c$ difference maps (Supplementary Fig. 3). In the earlier SR XRD structures of PS II[10,41–44] with a resolution lower than 3.0 Å it was difficult to locate them with confidence (especially the mobile Q_B) due to partial occupancy and quinone mobility.

The native XRD data indicate that there are no large-scale rearrangements of the Mn_4O_5Ca cluster and its protein environment between the different states (dark, 2F, 3F, and 3F′) in PS II. This is in line with Mn EXAFS data, which suggests that the largest possible changes in Mn-Mn distances upon S-state transitions are less than 0.5 Å (this estimate is based on the changes proposed in the S_2 to S_3 transition, if di-μ-oxo bridged Mn becomes mono-μ-oxo bridged)[20], which are well below the sensitivity of our current XRD measurements. To test the level of change detectable using our data we simulated a shift of the Mn_4CaO_5 cluster by 1 and 0.4 Å compared to the starting model based on SR data. In both cases a strong positive and negative peak corresponding to the shift was visible in the isomorphous difference density (Supplementary Fig. 10A,B), indicating that shifts of that magnitude should be detectable within the signal to noise level of the current data. In contrast when only perturbing the position of a single Mn within the Mn_4CaO_5 cluster by 0.5 Å, no clear peaks were observed in the difference density (Supplementary Fig. 10C), indicating that a structural change of such order can not be resolved at the present resolution. We furthermore evaluated the noise level in the current electron densities by computing the difference in position of the Mn_4CaO_5 cluster between the two monomers in each data set. For this approach we superimposed the $mFo-DFc$ fourier omit maps after simulated annealing (see Methods) for the two monomers and evaluated the differences between the OEC peak in these maps. The values are in the range of 0.3–0.6 Å, indicating that changes in Mn positions larger than about 0.5 Å should be visible in our data.

The height and volume of the anomalous XRD difference map peak of the OEC reflects the amount of data available for each S-state data set. Supplementary Fig. 9A shows that after scaling the anomalous difference densities of the 2F, 3F and 3F′ datasets individually at a sigma value of 80% of the peak maxima, the extent of the anomalous peak at the OEC is roughly similar for all data sets. It is also evident from this plot that the peak position of the anomalous signal for all datasets is in the vicinity of the center of mass of the four manganese, as expected for a signal originating from Mn. Before attempting to interpret the visible differences in the anomalous signal for the different S-states in terms of structural differences of the Mn_4CaO_5 cluster, it should be noted that at the present resolution the difference of the anomalous signal between two monomers in one PS II dimer is larger than the differences for the Mn_4CaO_5 cluster in the same monomer in different S-states. We quantified this by evaluating the difference in the peak position for the OEC between the two monomers for each of the datasets and found differences in the order of above 1 Å. This indicates that the noise level in our present anomalous data precludes the observation of the small changes expected between the different illumination states. Therefore analysis of detailed structural changes based on the anomalous signal of the OEC has to await higher data quality and in the light of the present data interpretations of structural changes can only be made using the isomorphous omit maps as these are derived from the full data for each flash state instead of only the anomalous data and consequently show lower noise levels.

We have used fs XES to follow the changes in the oxidation state of the Mn_4CaO_5 cluster on advancing from the S_3 to the S_0 state. The peak shift that was observed between the 2F and the 3F sample reproduced the shift in oxidation state between the highest oxidized (S_3 state) and most reduced state (S_0 state) found earlier[35]. Interestingly, the peak position of the spectrum observed at the transient time point, 250 μs after the 3rd flash, is very similar to that of the 2F spectrum. The observation that there is no significant change in the oxidation state of Mn within this time span is consistent with the kinetics of Mn oxidation/reduction in the $S_3 \rightarrow S_3Y_Z^{ox} \rightarrow S_4 \rightarrow S_0$ transition based on earlier time-resolved UV-VIS [45,46], EPR[47], IR spectroscopy[7] and Mn K-edge XAS[17] studies. It was inferred from these studies that a de-protonation step, forming a transient state $S_3Y_Z^{Ox}$, (also refered to as S_3')[7,46] occurs prior to Mn redox chemistry[7,46]. This lag phase before the onset of Mn redox chemistry was reported to be in the range of 100–250 μs[7,17]. Our results provide direct evidence that Mn redox chemistry does not occur within the first 250 μs after illumination of the S_3 state. This implies that the formation of a Mn^V species that has been invoked for a nucleophilic attack mechanism[2], or the formation of a peroxide intermediate which will result in Mn reduction[1], does not occur within the first 250 μs after the third flash. The formation of an oxygen radical species[4,6] within this time period cannot be excluded by our data (since no Mn oxidation would be involved), but is unlikely on the basis of the earlier UV-VIS data[45]. The long delay before the onset of Mn redox chemistry suggests that the formation of the $S_3Y_Z^{ox}$ state is not a simple deprotonation step. It is rather likely accompanied by slower structural changes of the Mn_4CaO_5 cluster and/or the protein framework[7] that are required to stabilize the deprotonated $S_3Y_Z^{ox}$ state of the OEC in the conformation necessary for subsequent O-O bond formation. In line with this conclusion, a recent report[46] underlined the importance of the exact structure of the H-bonding network for efficient turn over in the $S_3 \rightarrow S_3Y_Z^{ox} \rightarrow S_4 \rightarrow S_0$ transition by demonstrating that Ca/Sr

exchange in the OEC perturbs the H-bonding network and results in a significant slowing of the $S_3 \rightarrow S_3Y_Z^{ox}$ transition[4,46].

In summary, we have investigated the S-state intermediates and a transient state with fs XES/XRD by following the S-state transitions under ambient conditions. Advancement of S-states by *in situ* photoexcitation was confirmed by the O_2 evolution pattern and the XES spectral shifts. The XES data indicate that the Mn oxidation state does not change within 250 μs after the illumination of the S_3 state. The most likely explanation for this observation is that the deprotonation process of the OEC proceeds prior to the electron transfer, and the O-O bond formation occurs more than 250 μs after the 3rd photo-excitation, in agreement with previous studies[7,17,46,47]. Structural changes that are large enough to access with the current XRD resolution of 4.5–5.2 Å were not observed in the OEC, surrounding amino-acid residues, or the quinone sides upon the S_3, $S_3Y_Z^{ox'}$, and S_0 state formation, which implies that the structural changes in the OEC are within the order of ≤ 0.5Å. Interestingly, our room temperature structural data clearly show the presence of several features - although not interpretable at the present resolution –in the *mFo-DFc* difference electron density maps, indicating structural differences in the RT XFEL data compared to the previous SR cryogenic structural models. The future improvements in the crystal quality and data, especially the anomalous signal, will also allow us to use the XFEL approach to resolve the sequence of the important structural and electronic changes during the $S_3 \rightarrow S_3Y_Z^{ox} \rightarrow S_4 \rightarrow S_0$ transition, providing unprecedented experimental insights into the mechanism of photosynthetic water oxidation.

Methods

Sample Preparation

PS II was purified from *Thermosynechococcus elongatus* (*T. elongatus*) as described elsewhere[48]. Crystals that were obtained as described in [48] and a seed kit (Hampton Research, Ca, USA) were used to produce a PS II seed stock solution in buffer A (100 mM PIPES pH 7, 5 mM $CaCl_2$, 6% (w/w) PEG 2000, 0.03% β-dodecyl maltoside (βDM)) for microcrystallization of PS II. Microcrystals of PS II were obtained by mixing aliquots of the PS II seed stock solution with PS II solution (chlorophyll (Chl) concentration 4 mM, corresponding to a protein concentration of ~ 40 mg/ml) in a 1:4 ratio. Box shaped crystals (5–10 μm in the longest dimension, 5 μm in the shorter dimension) were suspended in buffer C (100 mM MES pH 6.5, 5 mM $CaCl_2$, 10% (w/v) PEG2000, 30% (w/v) glycerol). The final concentration of the crystal suspension was determined by measuring Chl concentration of small aliquots of the suspension, dissolved in 80% acetone[49]. The Chl concentration was adjusted between 0.3 and 0.5 mM, corresponding to a protein concentration of 8.5–14 μM (3–5 mg/ml). For solution samples the purified PS II was resuspended in buffer D (100 mM MES, pH 6.5, 5 mM $CaCl_2$, 0.015% βDM, 1.3 M sucrose) to a final protein concentration of 80–90 mg/ml.

Thermolysin was obtained from Hampton Research (Ca, USA). Microcrystals of thermolysin were obtained as described previously[28] using PEG2000 as precipitant.

Membrane-Inlet Mass Spectrometry Measurements

Sample suspensions of PS II from *T. elongatus* of 8 mg/ml Chl were diluted to 7 mg/ml Chl with $H_2^{18}O$ (98%) to give a final enrichment of $H_2^{18}O$ of about 12% and final salt concentrations of 4.4 mM $CaCl_2$, 85 mM MES and 1.1 M Sucrose. No electron acceptors were added. The ^{18}O-enriched samples were loaded into a gas-tight Hamilton syringe and pumped through a silicon capillary (ID = 50 μm, OD 160 μm) into another gas tight Hamilton syringe that collected the sample. Both syringes were placed on separate syringe pumps. Samples were kept in darkness or very dim green light during all steps, except when illuminated inside the capillary with laser light travelling through 1–4 optical fibers (400 μm core diameter) directly attached to a region of the capillary with the polyimide coating removed. This setup directly mirrors the in-capillary illumination set up for the CXI experiment (see Fig. 1A and below).

The oscillation pattern of PS II crystals was obtained in the same way, but the experimental details were as follows: the PS II crystal suspension was concentrated to 3.2 mM Chl and was then diluted with $H_2^{18}O$ (98%) to 2.5 mM Chl to give a final enrichment of 21.5 %. The final concentrations of other additions were 5 mM $CaCl_2$, 80 mM MES, 1.2 M sucrose and 11% PEG2000. The capillary that was used to conduct these experiments had an inner diameter (ID) of 100 μm and an outside diameter (OD) of 360 μm.

A Nd:YAG laser (Continuum Inlite II-20, 532 nm, 7 ns pulse width) was used for sample illumination. To obtain a stable output intensity of 7 μJ/fiber (intensities of individual flashes may vary by ±5%), the laser was operated continuously at 20 Hz. The illumination periods were set with the help of a fast shutter (SH05 operated with SC10 Controller; both Thorlabs), while the flash frequency was controlled via the Q-switch divider (20Hz or 10Hz).

The oxygen produced was quantified by injecting the illuminated sample into a membrane-inlet cell containing 600 μl water, connected via a Si membrane (Mem 213) and a cooling trap (dry ice/ethanol) to an isotope ratio mass spectrometer (DELTA V, ThermoFinnigan)[50]. The O_2 formed during illumination was detected with excellent S/N ratio as the non-labeled $^{16}O^{16}O$, the mixed labeled $^{16}O^{18}O$ and double-labeled $^{18}O^{18}O$ species. In order to obtain a flash pattern, the light-induced yields for O_2 production (detected at m/z = 34) obtained with (x-1) illuminations were subtracted from that with x illuminations. For the first flash the background $^{34}O_2$ signal of a non-illuminated sample was subtracted. Each measurement was repeated twice (deviation of the points were within 10%).

Determination of the total O_2 produced per PS II complex

Determination of the total O_2 produced per PS II complex and flash number requires the absolute calibration of the MIMS signals. This calibration was achieved by the injection of known volumes of air-saturated water into the MIMS cell. This value was used to determine the micromoles of O_2 produced by PS II by the illumination with 3 flashes using 7μJ/fiber measured in a silica capillary (ID = 75 μm, OD 160 μm), with a flow rate of 0.5 μl/min and a flash frequency of 4 Hz. To account for diffusion losses of $^{34}O_2$ out of the capillary during the flow of the sample a loss factor was determined separately by measuring the O_2 content

of a PS II sample that was illuminated inside a gas tight syringe by 50 consecutive Xenon lamp flashes (2 Hz frequency, in the presence of acceptors) and either directly injected into the MIMS cell or first flowed through the capillary setup used for the flash measurements into the collection syringe and then injected into the MIMS cell.

After correcting the O_2 amount obtained in the 3 flash experiment by the loss factor this number was then divided by the μmole of PS II reaction center, which resulted in about 0.73 O_2/RC. Since 3 consecutive flashes are required to produce one molecule of oxygen in a dark-adapted PS II reaction center, a maximum of one O_2/reaction center can be expected under these conditions. The above number of 73% oxygen yield directly translates into light saturation. For 100% light saturation we would expect a value of 73% (0.9^3), since even under stationary conditions an average 'miss' of 10% occurs due to charge equillibria within PS II.

Sample Injection and Illumination at CXI

Samples were injected into the CXI instrument chamber[32] using an electrospun liquid microjet[28]. Aliquots of 50–150 μl of sample were placed in a microcentrifuge tube placed inside the pressurized cell with a Pt-electrode and the end of the injector capillary submerged in the sample. Pressures of 17–20 psi against the CXI chamber pressure (10^{-4} Torr) and voltages of around 3000 V were applied depending on the buffer composition and crystal concentration. The injector capillary was a clear silica capillary with an ID of 75 or 100 μm and an OD of 150 μm or 360 μm, respectively. The flow rate was in the range of 0.25–1.0 μl/min (for the 75 μm ID capillary) and 1.2–3.5 μl/min (for the 100 μm ID capillary) depending on the sample viscosity and the backing pressure. We measured the flow rate from the mass of sample consumed divided by the run time (data quoted here was obtained this way), and in several cases we also estimated the flow rate from the velocity of crystals flowing in the capillary by using in-capillary visualization of the flow via a microscope mounted camera. To ensure that the samples were in the dark stable S_1 state before injection, all sample handling and storage was performed in darkness or under dim green light. For visualization of the jet an IR laser diode (Coherent Lasiris, 785nm, 15 mW) was used (see ref. [28] for details). The wavelength was chosen to be outside the absorption spectrum of PS II.

Sample illumination for advancement into higher S-states was conducted using the output of a frequency doubled Nd:YLF laser at 527 nm (Coherent Evolution) with 150 ns pulse duration. The light from the laser was coupled into multi-mode fiber light guides with a core diameter of 400 μm. Three of these light guides (laser 1, 2 and 3 in Fig. 1A) were directly coupled onto the silica capillary of the sample injector, and an additional laser (laser 4 in Fig. 1A) illuminated the sample in the jet. The output of all three fibers was equalized to 10 μJ/pulse (1.4 times the power necessary for saturation of the oxygen production in our off-line O_2 flash yield experiments, see above) using wave plates and the transmission profile and output power of all fibers was measured before the experiment and after each change to the experimental setup. The center-center distance between the fibers was 1.98 mm and typical illumination parameters for a 75 um ID capillary (1 μl/min flow rate, 8.9 Hz illumination frequency) result in a delay between the pump laser flashes on the same volume

segment of 0.52 s. To generate 2F samples (enriched in the S_3 state) lasers 2 and 3 were used, and the sample reached the X-ray interaction region about 0.5 s after the 2nd pump laser flash. To generate 3F samples (enriched in the S_0 state), lasers 1, 2 and 3 were used and the sample reached the X-ray interaction region about 0.5 s after the 3rd pump laser flash. Finally, to study transients during the S_3 to S_0 transition, lasers 2 and 3 (for advancing the sample from the S_1 to the S_3 state) in combination with laser 4 (to start the transition from the S_3 to the S_0 state) were used. In this experiment the time delay of the X-ray probe with respect to the laser 4 was set to 250 μs giving rise to the 3F′ data (enriched in the $S_3Y_Z^{ox}$ state).

CXI Instrument and X-ray Parameters

The CXI instrument of LCLS[32] was used in the 1 μm focus setting with the beam being focused to 1.5×1.5 μm^2 full width half maximum using Kirkpatrick-Baez mirrors[51]. The pulse length used was about 45 fs and the repetition rate was 120 Hz. The energy was varied between 7.1 and 9.7 keV with $3–6\times10^{11}$ photons/pulse. The dose therefore varied between 50 and 300 MGy. XES was measured using 7.1 keV excitation, due to the higher cross section for the Mn transition at this energy. XRD of PS II was measured at both energies but no difference in diffraction quality between the two energies was observed. The majority of the PS II XRD data was obtained with incident energy of 7.1 keV. XRD of thermolysin was collected at 9.7 keV (above the Zn edge).

X-ray Emission Spectroscopy Setup

X-ray emission spectra were recorded in a shot-by-shot mode using a custom-built spectrometer in the von Hamos geometry[25,52]. The crystal analyzer array was located 500 mm from the interaction point and with an angle of 81° between the center of the array and the X-ray beam. A set of 16 Si(440) crystal analyzers was used and the Bragg angle range was 85.9° to 83.4°, equivalent to an energy range from 6473.8 to 6500 eV (limited by the detector size). The signal was recorded on a 140k CSPAD[53,54], located below the interaction region. The setup was calibrated by recording spectra from solutions of $Mn^{II}Cl_2$ as previously described[25]. The first moment values of the emission spectra were calculated between 6486 and 6494 eV as described [35]. Before computing difference spectra the flash state spectra were smoothed by using either a moving average over a 0.5 eV window or by fitting a cubic polynomial of 3 eV width to each data point.

SR XES spectra were recorded at ESRF beam line ID 26 using the 440 reflection of five spherically bent (R= 1000 mm) Si crystal analyzers in combination with a silicon drift detector aligned in a Rowland geometry. The overall energy bandwidth of the X-ray emission spectrometer was 0.8 eV. The sample was kept at 15K in a liquid He cryostat surrounded by He as a heat exchange gas. The ESRF storage ring was run in 16 bunch mode with ring currents between 60 and 90 mA. The incident beam was monochromatized and tuned to 6.75 keV using the 111 reflection of a pair of cryogenically cooled Si crystals. The beam size was 1.0 (h) $\times$ 0.2 (v) mm^2 and the beam position on the sample was changed after 1 second of X-ray illumination.

Computational Facilities

Over a five-day period, 114 TB data were collected at LCLS, grouped into five 12-hr shifts. Data were processed immediately in order to assess their completeness and quality. However, since the data size exceeded the processing capacity of the 480-core Linux cluster available at LCLS, arrangements were made to access an additional 1000 Linux cores at the National Energy Research Scientific Computing Center (NERSC). Transfer of the data from SLAC to NERSC was made over the Energy Sciences Network (ESnet) at a maximum sustained rate of 7.5 Gb s^{-1}.

XRD Data Processing

X-ray diffraction data were recorded using the large CSPAD at LCLS's CXI instrument[32], and processed using *cctbx.xfel*[55,56]. A dark-current image (pedestal) was subtracted from each image prior to data reduction. An initial triage step was evaluated, retaining only those images containing 16 or more strong, low-resolution Bragg spots as determined by the *Spotfinder* procedure[56,57]. However, it was found that this step rejected some useful data, so it was ultimately omitted from the data processing protocol. Indexing (determination of the unit cell and crystal orientation) was performed with the LABELIT implementation[58] of the Rossmann DPS algorithm[59,60], and was guided by supplying the known unit cell[61,62]. Where more than one crystal was exposed in the same shot, indexing was attempted on the two most dominant lattices[56]. The number of images or lattices retained after each processing step is detailed in Supplementary Table 1.

Crystal orientations determined by LABELIT were optimized by minimizing the positional difference between the observed Bragg spots and those predicted by the model. Orientational models were further refined so that minimal perturbations were needed to exactly fit the observed Bragg spots to Bragg's law, under the simplifying assumptions of a perfect crystal lattice and a monochromatic beam. Differences between this idealized model and the actual set of observations then allowed us to estimate crystal properties such as mosaicity and the average size of coherently scattering mosaic blocks, leading to a realistic model of Bragg spot positions suitable for signal integration.

Intensities were integrated by summation within a spot mask derived from nearby strong spots atop a planar background[63,64] and corrected for polarization[65]. Intensity variances, $\sigma^2(I)$, were derived by counting statistics[66] and a coarse estimate of the detector gain. Error estimates from each diffraction pattern were then inflated by assuming that negative values of $I/\sigma(I)$ are actually decoy measurements (noise only) with a Gaussian distribution centered at zero and with a standard deviation of 1, thus providing a lower bound on modeling errors. A separate resolution cutoff was determined for each image based on a Wilson plot (average intensity vs. binned resolution).

Integrated, non-negative intensities from separate images were then scaled to intensities derived from isomorphous reference structures (PDB codes 3bz1 and 3bz2 for PS II[12]; PDB code 2tli for thermolysin[37]), without separately accounting for the partiality fraction of each observation. Images whose intensities correlated poorly (10%) with those of the reference model were rejected, as were images that deviated from the reference unit cell lengths (10%)

or angles (2°), or that did not obey the expected symmetry. Multiple measurements with the same Miller index were merged by averaging, and the error was modeled by propagating the σ(*I*) values in quadrature. The resolution cutoff for the merged data sets was determined from the resolution-dependence both of the multiplicity, and of $CC_{1/2}$, the correlation coefficient of semi-datasets merged from odd- and even-numbered images[36]. The expected contribution of the anomalous signal to |F| was estimated using the Web server of the Biomolecular Structure Center at University of Washington (http://skuld.bmsc.washington.edu/scatter/AS_index.html).

Phasing and Refinement

As a starting PSII model, we used PDB IDs 3bz1 and 3bz2[12], modified to include all atoms in the OEC based on the high-resolution structure 3arc[13], and re-refined against the 3bz1/3bz2 deposited amplitudes in *phenix.refine*[67]. The structure was then reduced to a single copy of the PS II complex and the processed datasets were phased by molecular replacement in Phaser[68]. Refinement of coordinates and B-factors was performed in *phenix.refine* using tight restraints including two-fold non-crystallographic symmetry, with the distances between heavy atoms in the OEC restrained to the values determined by EXAFS[20]. Simulated annealing omit maps were generated with the OEC atoms set to zero occupancy, with harmonic restraints[69] applied to the OEC and surrounding atoms; the default parameters of a starting temperature of 5000K and 100K steps were used. Isomorphous difference maps were generated using *phenix.fobs_minus_fobs_map*. Structures and maps were aligned using the *PHENIX* structure comparison tool. All structure figures were created in *PyMOL* 1.2.

The thermolysin structure was solved by molecular replacement using PDB ID 2tli[37] with metals and waters removed, rebuilt using the *PHENIX AutoBuild* wizard[70], and refined in *phenix.refine*. Simulated annealing omit maps were generated as for PS II, with Zn and Ca occupancies set to zero.

Supplementary Material

Refer to Web version on PubMed Central for supplementary material.

Acknowledgments

References

1. Renger G. Light induced oxidative water splitting in photosynthesis: Energetics, kinetics and mechanism. J Photochem Photobiol B. 2011; 104:35–43. [PubMed: 21454089]

2. Brudvig GW. Water oxidation chemistry of photosystem II. Phil Trans Roy Soc B. 2008; 363:1211–1218. [PubMed: 17954436]

3. Kok B, Forbush B, McGloin M. Cooperation of charges in photosynthetic oxygen evolution. I. A linear four step mechanism. Photochem Photobiol. 1970; 11:457–475. [PubMed: 5456273]

4. Cox N, Messinger J. Reflections on substrate water and dioxygen formation. Biochim Biophys Acta. 2013; 1827:1020–1030. [PubMed: 23380392]

5. Yano J, et al. Where water is oxidized to dioxygen: Structure of the photosynthetic Mn_4Ca cluster. Science. 2006; 314:821–825. [PubMed: 17082458]

6. Yano J, Yachandra VK. Where water is oxidized to dioxygen: Structure of the photosynthetic Mn_4Ca cluster from X-ray spectroscopy. Inorg Chem. 2008; 47:1711–1726. [PubMed: 18330965]

7. Noguchi T, Suzuki H, Tsuno M, Sugiura M, Kato C. Time-resolved infrared detection of the proton and protein dynamics during photosynthetic oxygen evolution. Biochemistry. 2012; 51:3205–3214. [PubMed: 22458839]

8. Haddy A. EPR spectroscopy of the manganese cluster of photosystem II. Photosynth Res. 2007; 92:357–368. [PubMed: 17551843]

9. Cox N, Pantazis DA, Neese F, Lubitz W. Biological water oxidation. Acc Chem Res. 2013; 46:1588–1596. [PubMed: 23506074]

10. Ferreira KN, Iverson TM, Maghlaoui K, Barber J, Iwata S. Architecture of the photosynthetic oxygen-evolving center. Science. 2004; 303:1831–1838. [PubMed: 14764885]

11. Loll B, Kern J, Saenger W, Zouni A, Biesiadka J. Towards complete cofactor arrangement in the 3.0 Å resolution structure of photosystem II. Nature. 2005; 438:1040–1044. [PubMed: 16355230]

12. Guskov A, et al. Cyanobacterial photosystem II at 2.9-A resolution and the role of quinones, lipids, channels and chloride. Nat Struct Mol Biol. 2009; 16:3343–42.

13. Umena Y, Kawakami K, Shen JR, Kamiya N. Crystal structure of oxygen-evolving photosystem II at a resolution of 1.9 angstrom. Nature. 2011; 473:55–60. [PubMed: 21499260]

14. Siegbahn PEM. Structures and energetics for O_2 formation in photosystem II. Acc Chem Res. 2009; 42:1871–1880. [PubMed: 19856959]

15. Sproviero EM, McEvoy JP, Gascon JA, Brudvig GW, Batista VS. Computational insights into the O_2-evolving complex of photosystem II. Photosynth Res. 2008; 97:91–114. [PubMed: 18483777]

16. Yamaguchi K, et al. Full geometry optimizations of the mixed-valence $CaMn_4O_4X(H_2O)_4$ (X=OH or O) cluster in OEC of PS II: Degree of symmetry breaking of the labile Mn-X-Mn bond revealed by several hybrid DFT calculations. Int J Quantum Chem. 2013; 113:525–541.

17. Haumann M, et al. Photosynthetic O_2 formation tracked by time-resolved X-ray experiments. Science. 2005; 310:1019–1021. [PubMed: 16284178]

18. Yano J, et al. X-ray damage to the Mn₄Ca complex in single crystals of photosystem II: A case study for metalloprotein crystallography. Proc Natl Acad Sci USA. 2005; 102:12047–12052. [PubMed: 16103362]

19. Grabolle M, Haumann M, Müller C, Liebisch P, Dau H. Rapid loss of structural motifs in the manganese complex of oxygenic photosynthesis by x-ray irradiation at 10–300 K. J Biol Chem. 2006; 281:4580–4588. [PubMed: 16352605]

20. Glöckner C, et al. Structural changes of the oxygen evolving complex in photosystem II during the catalytic cycle. J Biol Chem. 2013; 288:22607–22620. [PubMed: 23766513]

21. Kern J, et al. Simultaneous femtosecond X-ray spectroscopy and diffraction of photosystem II at room temperature. Science. 2013; 340:491–495. [PubMed: 23413188]

22. Neutze R, Wouts R, van der Spoel D, Weckert E, Hajdu J. Potential for biomolecular imaging with femtosecond X-ray pulses. Nature. 2000; 406:752–757. [PubMed: 10963603]

23. Chapman HN, et al. Femtosecond X-ray protein nanocrystallography. Nature. 2011; 470:73–77. [PubMed: 21293373]

24. Boutet S, et al. High-resolution protein structure determination by serial femtosecond crystallography. Science. 2012; 337:362–364. [PubMed: 22653729]

25. Alonso-Mori R, et al. Shot-by-shot energy-dispersive X-ray emission spectroscopy using an X-ray free electron laser. Proc Natl Acad Sci USA. 2012; 109:19103–19107. [PubMed: 23129631]

26. Glatzel P, Bergmann U. High resolution 1s core hole X-ray spectroscopy in 3d transition metal complexes - electronic and structural information. Coord Chem Rev. 2005; 249:65–95.

27. Kern J, et al. Room temperature femtosecond X-ray diffraction of photosystem II microcrystals. Proc Natl Acad Sci U S A. 2012; 109:9721–9726. [PubMed: 22665786]

28. Sierra RG, et al. Nanoflow electrospinning serial femtosecond crystallography. Acta Cryst D. 2012; 68:1584–1587. [PubMed: 23090408]

29. de Wijn R, van Gorkom HJ. Kinetics of electron transfer from Q(a) to Q(b) in photosystem II. Biochemistry. 2001; 40:11912–11922. [PubMed: 11570892]

30. Krivanek R, Kern J, Zouni A, Dau H, Haumann M. Spare quinones in the Q(B) cavity of crystallized photosystem II of *Thermosynechococcus elongatus*. Biochim Biophys Acta. 2007; 1767:520–527. [PubMed: 17397795]

31. Shevela D, Messinger J. Probing the turnover efficiency of photosystem II membrane fragments with different electron acceptors. Biochim Biophys Acta. 2012; 1817:1208–1212. [PubMed: 22503842]

32. Boutet S, Williams JG. The Coherent X-ray Imaging (CXI) instrument at the Linac Coherent Light Source (LCLS). New J Phys. 2010; 12:035024.

33. Iuzzolino L, Dittmer J, Dörner W, Meyer-Klaucke W, Dau H. X-ray absorption spectroscopy on layered photosystem II membrane particles suggests manganese-centered oxidation of the oxygen-evolving complex for the S_0-S_1, S_1-S_2, and S_2-S_3 transitions of the water oxidation cycle. Biochemistry. 1998; 37:17112–17119. [PubMed: 9860823]

34. Kulik LV, Epel B, Lubitz W, Messinger J. Electronic structure of the Mn_4O_xCa cluster in the S_0 and S_2 states of the oxygen-evolving complex of photosystem II based on pulse Mn^{55}-ENDOR and EPR spectroscopy. J Am Chem Soc. 2007; 129:13421–13435. [PubMed: 17927172]

35. Messinger J, et al. Absence of Mn-centered oxidation in the S_2 -> S_3 transition: Implications for the mechanism of photosynthetic water oxidation. J Am Chem Soc. 2001; 123:7804–7820. [PubMed: 11493054]

36. Karplus PA, Diederichs K. Linking crystallographic model and data quality. Science. 2012; 336:1030–1033. [PubMed: 22628654]

37. English AC, Done SH, Caves LSD, Groom CR, Hubbard RE. Locating interaction sites on proteins: The crystal structure of thermolysin soaked in 2% to 100% isopropanol. Proteins. 1999; 37:628–640. [PubMed: 10651278]

38. Barends TR, et al. Anomalous signal from S atoms in protein crystallographic data from an X-ray free-electron laser. Acta Cryst D. 2013; 69:838–842. [PubMed: 23633593]

39. Barends TR, et al. De novo protein crystal structure determination from X-ray free-electron laser data. Nature. 2013; 505:244–247. [PubMed: 24270807]

40. Ferrer JL, Larive NA, Bowler MW, Nurizzo D. Recent progress in robot-based systems for crystallography and their contribution to drug discovery. Expert Opin Drug Discov. 2013; 8:835–847. [PubMed: 23656378]

41. Zouni A, et al. Crystal structure of photosystem II from *Synechococcus elongatus* at 3.8 angstrom resolution. Nature. 2001; 409:739–743. [PubMed: 11217865]

42. Biesiadka J, Loll B, Kern J, Irrgang KD, Zouni A. Crystal structure of cyanobacterial photosystem II at 3.2 angstrom resolution: a closer look at the Mn-cluster. Phys Chem Chem Phys. 2004; 6:4733–4736.

43. Kamiya N, Shen JR. Crystal structure of oxygen-evolving photosystem II from *Thermosynechococcus vulcanus* at 3.7-Å resolution. Proc Natl Acad Sci U S A. 2003; 100:98–103. [PubMed: 12518057]

44. Kern J, et al. Cyanobacterial photosystem II at 3.2 Å resolution - the quinone binding pockets. Photosynth Res. 2005; 84:153–159. [PubMed: 16049768]

45. Rappaport F, Blancharddesce M, Lavergne J. Kinetics of electron-transfer and electrochromic change during the redox transitions of the photosynthetic oxygen-evolving complex. Biochim Biophys Acta. 1994; 1184:178–192.

46. Rappaport F, Ishida N, Sugiura M, Boussac A. Ca^{2+} determines the entropy changes associated with the formation of transition states during water oxidation by photosystem II. Energ Environ Sci. 2011; 4:2520–2524.

47. Razeghifard MR, Pace RJ. EPR kinetic studies of oxygen relaese in thylakoids in PSII membranes: A kinetic intermediate in the S_3 to S_0 transition. Biochemistry. 1999; 38:1252–1257. [PubMed: 9930985]

48. Kern J, et al. Purification, characterisation and crystallisation of photosystem II from *Thermosynechococcus elongatus* cultivated in a new type of photobioreactor. Biochim Biophys Acta. 2005; 1706:147–157. [PubMed: 15620375]

49. Porra RJ, Thompson WA, Kriedemann PE. Determination of accurate extinction coefficients and simultaneous equations for assaying chlorophylls a and b extracted with four different solvents: verification of the concentration of chlorophyll standards by atomic absorption spectroscopy. Biochim Biophys Acta. 1989; 975:384–394.

50. Beckmann K, Messinger J, Badger MR, Wydrzynski T, Hillier W. Online mass spectrometry: membrane inlet sampling. Photosynth Res. 2009; 102:511–522. [PubMed: 19653116]

51. Siewert F, et al. Ultra-precise characterization of LCLS hard X-ray focusing mirrors by high resolution slope measuring deflectometry. Opt Express. 2012; 20:4525–4536. [PubMed: 22418212]

52. Alonso-Mori R, et al. A multicrystal wavelength dispersive X-ray spectrometer. Rev Sci Instrum. 2012; 83:073114. [PubMed: 22852678]

53. Hart P, et al. The CSPAD megapixel x-ray camera at LCLS. Proc SPIE. 2012; 8504:85040C–85041.

54. Herrmann S, et al. Cspad-140k: A versatile detector for LCLS experiments. Nucl Instrum Meth A. 2013; 718:550–553.

55. Sauter NK, Hattne J, Grosse-Kunstleve RW, Echols N. New Python-based methods for data processing. Acta Cryst D. 2013; 69:1274–1282. [PubMed: 23793153]

56. Hattne J, et al. Accurate macromolecular structures using minimal measurements from X-ray free-electron lasers. Nature Methods. 2014; 11:545–548. [PubMed: 24633409]

57. Zhang Z, Sauter NK, van den Bedem H, Snell G, Deacon AM. Automated diffraction image analysis and spot searching for high-throughput crystal screening. J App Crystallogr. 2006; 39:112–119.

58. Sauter NK, Grosse-Kunstleve RW, Adams PD. Robust indexing for automatic data collection. J App Crystallogr. 2004; 37:399–409.

59. Steller I, Bolotovsky R, Rossmann MG. An algorithm for automatic indexing of oscillation images using Fourier analysis. J App Crystallogr. 1997; 30:1036–1040.

60. Rossmann MG, van Beek CG. Data processing. Acta Cryst D. 1999; 55:1631–1640. [PubMed: 10531511]

61. Paithankar KS, et al. Simultaneous X-ray diffraction from multiple single crystals of macromolecules. Acta Cryst D. 2011; 67:608–618. [PubMed: 21697599]

62. White TA, et al. Crystallographic data processing for free-electron laser sources. Acta Cryst D. 2013; 69:1231–1240. [PubMed: 23793149]

63. Otwinowski, Z.; Minor, W. Macromolecular Crystallography, part A. Vol. 276. Academic Press; 1997. Processing of X-ray diffraction data collected in oscillation mode.

64. Leslie AG. Integration of macromolecular diffraction data. Acta Cryst D. 1999; 55:1696–1702. [PubMed: 10531519]

65. Kahn R, et al. Macromolecular crystallography with synchrotron radiation - photographic data-collection and polarization correction. J App Crystallogr. 1982; 15:330–337.

66. Leslie AG. The integration of macromolecular diffraction data. Acta Cryst D. 2006; 62:48–57. [PubMed: 16369093]

67. Afonine PV, et al. Towards automated crystallographic structure refinement with phenix.refine. Acta Cryst D. 2012; 68:352–367. [PubMed: 22505256]

68. McCoy AJ, et al. Phaser crystallographic software. J App Crystallogr. 2007; 40:658–674.

69. Hodel A, Kim SH, Brunger AT. Model bias in macromolecular crystal-structures. Acta Cryst A. 1992; 48:851–858.

70. Terwilliger TC, et al. Iterative model building, structure refinement and density modification with the PHENIX AutoBuild wizard. Acta Cryst D. 2008; 64:61–69. [PubMed: 18094468]
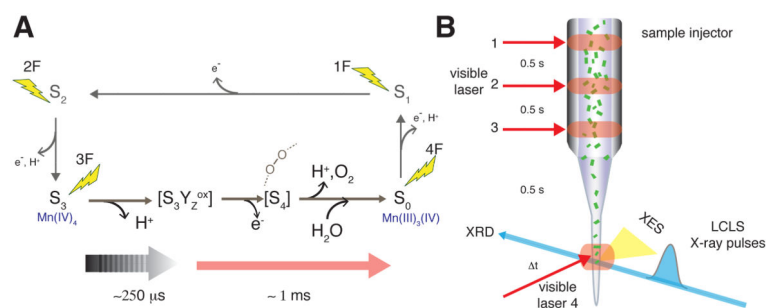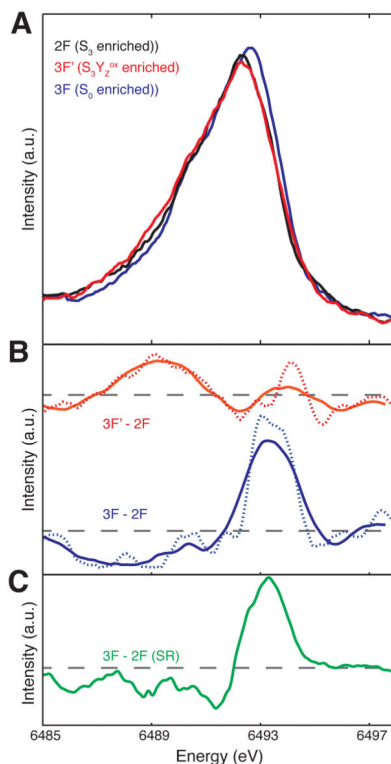
Figure 1.
Flash-induced changes in PS II and experimental setup used at LCLS A) Kok-cycle describing the different stable intermediate states of the catalytic water oxidation reaction in PS II. B) Scheme for the illumination setup used to advance PS II in the catalytic cycle and measure simultaneously the XRD and XES signal at LCLS. Lasers 2 and 3 were used to generate 2F samples, lasers 1, 2, 3 for 3F samples and lasers 2, 3 and 4 to generate the 3F′ samples.
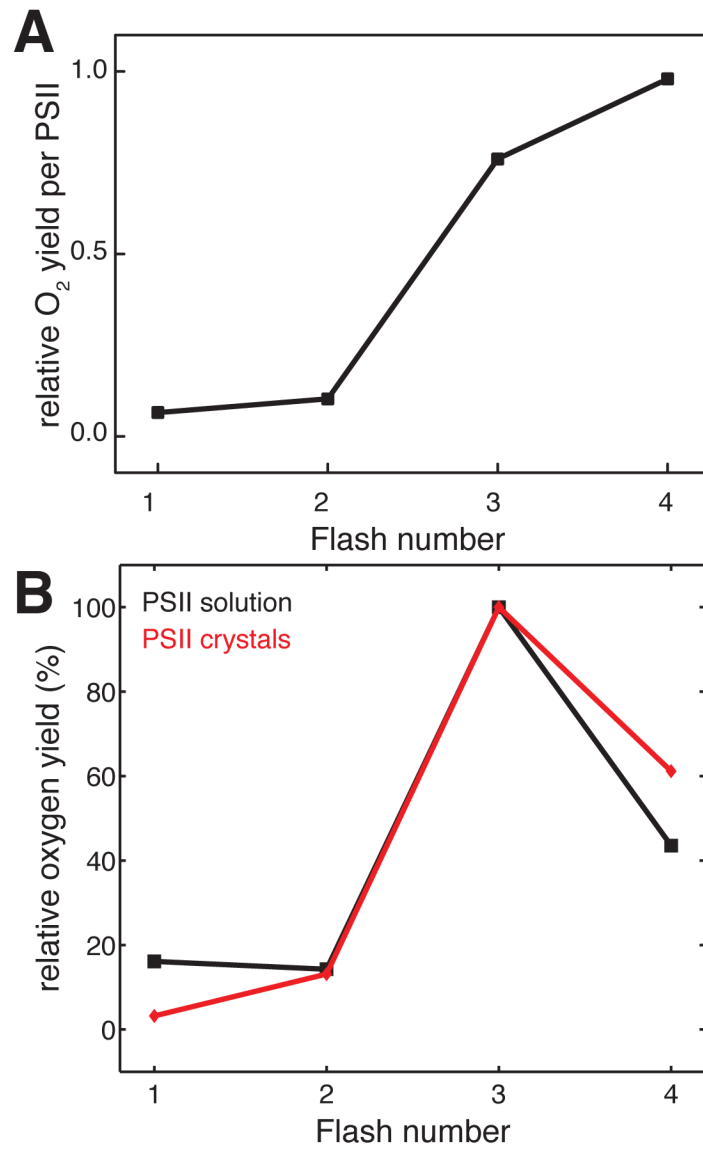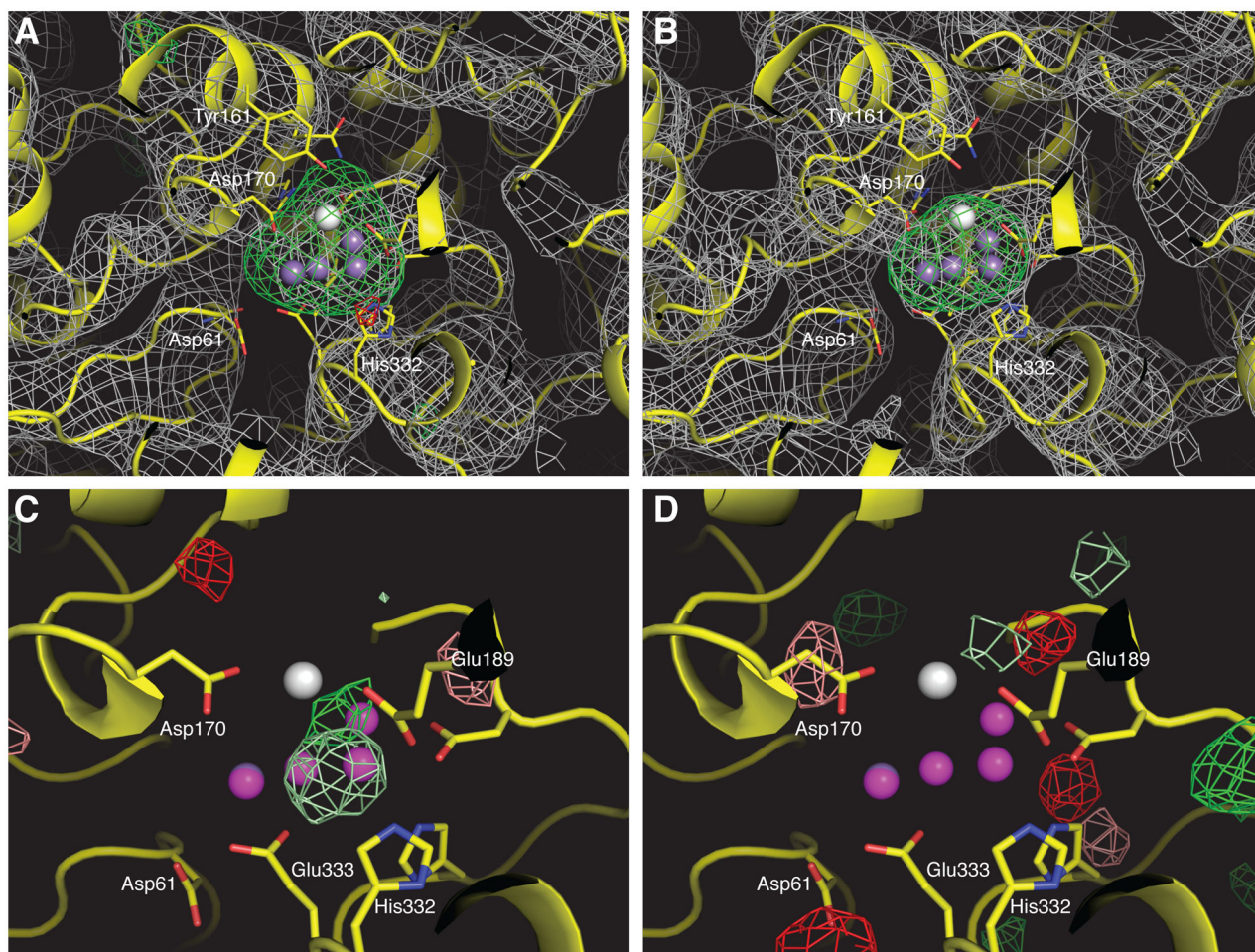
Figure 2.
Oxygen production by PSII A) Relative O_2 yield per PSII as detected by MIMS as a function of flash number (measurement shown is for PS II solutions, flow rate 0.5 μl/min, frequency 4 Hz, light intensity was 7 μJ for each fiber). B) O_2 yield measured by MIMS as a function of flash number from PS IIsolutions (black) and PS II microcrystals (red).
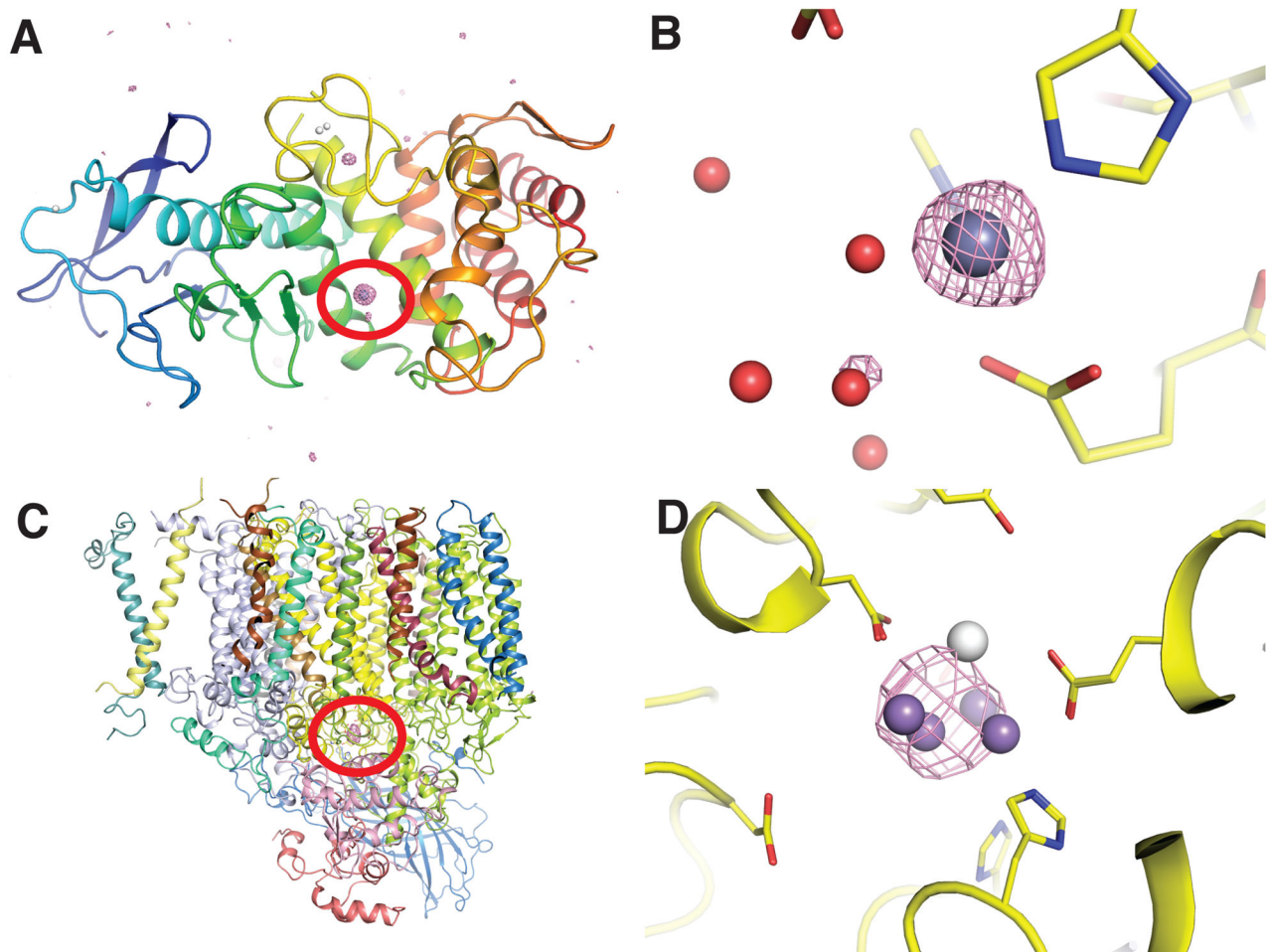
Figure 3.
Mn Kβ XES of PS II A) XES recorded with <50 fs X-ray pulses at LCLS. Spectra were measured 0.5 s after two laser flashes (2F, black; lasers 2 and 3 on), or 0.5 s after three laser flashes (3F, blue; lasers 1, 2, and 3 on), and ~250 μs after three laser flashes (3F′, red; lasers 2, 3, and 4 on), respectively. B) Difference between the Mn Kβ XES of PS II, blue: 3F – 2F; red: 3F′ – 2F. Before calculating the difference curves, spectra were smoothed by moving average (dotted line) or cubic polynomial fitting (solid line, similar to the procedure used for analyzing the synchrotron data). (C) the 3F – 2F difference spectrum (green) from SR data collected at 15 K.
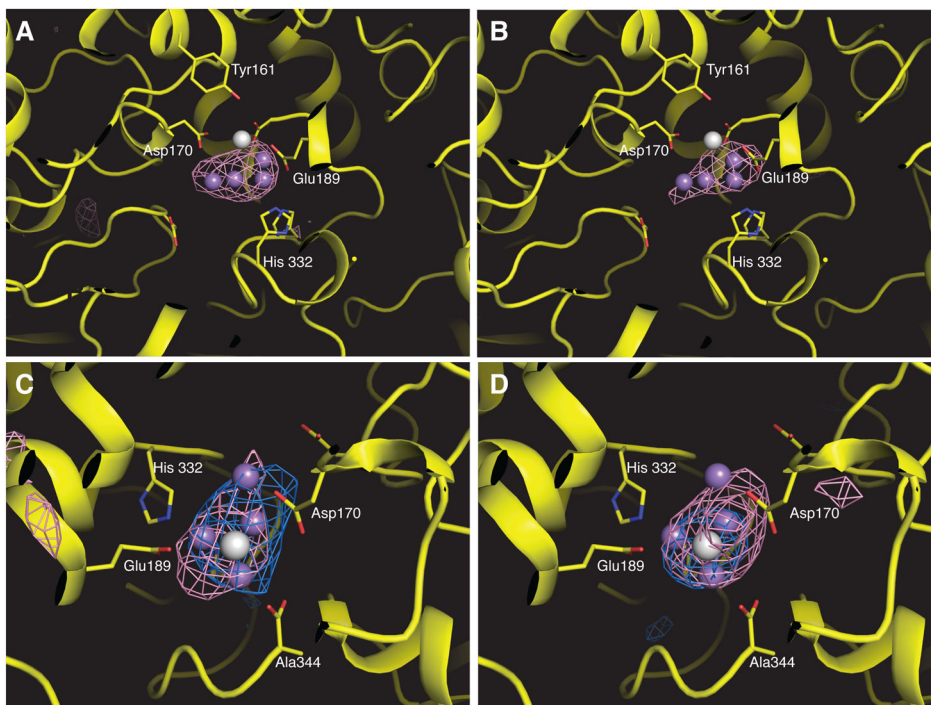
Figure 4.
Electron density maps obtained for PS II A) $2mF_o–DFs_c$ maps for the dark and B) the 2F data of PS II are shown in grey contoured at 1.0σ, $mF_o–DF_c$ maps after omitting the OEC are shown in green and red, contoured at +/−5.0σ. C) $mF_o\text{-}mF_o$ isomorphous difference maps for the 2F – dark data and D) the 3F – 2F data are shown for both monomers and are contoured at +3σ (bright green, monomer I; pale green, monomer II) and −3σ (red, monomer I; salmon, monomer II) together with the model for the 2F data.

Figure 5.
Anomalous signal in the XFEL data sets A) Anomalous difference map of the thermolysin data after simulated annealing with the occupancy for Zn and Ca set to zero to minimize model bias. The map is contoured at 4.0σ, extending over the entire thermolysin molecule. The position of the highest peak in the map (Zn atom) is highlighted. B) The same anomalous difference map of thermolysin shown in the region of the natively bound Zn ion, contour level at 3.0σ. C) Anomalous difference map obtained from the 3F data of PS II, shown for one monomer, location of the strongest peak is highlighted, contour level at 4.0σ. D) Enlarged view of the 3F anomalous density for the region of the OEC (contoured at 4.0σ). All maps shown are anomalous difference simulated annealing omit maps.

Figure 6.
Anomalous signal from Mn for different illumination states of PS II A) Anomalous map of the OEC in PS II is shown for the 2F data (magenta) in monomer I. (B) Anomalous map of the 3F data in monomer I. (C) Anomalous map of the 2F (cyan) and 3F (magenta) data in monomer I, orientation is rotated by 90° around horizontal and vertical axis compared to the view in A. (D) Anomalous map for monomer II, 2F (cyan) and 3F (magenta) data are shown, view direction is similar to panel C. All maps shown are anomalous difference simulated annealing omit maps contoured at 3σ.

Table 1

Statistics for processed data and refined structures

	Dark (S_1)	2-flash (2F)	3-flash + 250µs ($3F'$)	3-flash + 500ms (3F)	thermolysin
Wavelength	1.77 Å				1.27 Å
Resolution range (Å)	72.93 - 4.9 (5.08 - 4.9)	72.97 - 4.5 (4.66 - 4.5)	68.41 - 5.2 (5.39 - 5.2)	72.96 - 4.6 (4.76 - 4.6)	34.27 - 1.80 (1.86 - 1.80)
Space group	$P\ 2_12_12_1$	$P\ 2_12_12_1$	$P\ 2_12_12_1$	$P\ 2_12_12_1$	$P\ 6_122$
Unit cell dimensions	132.9	132.3	132.6	132.4	93.0
	229.0	228.7	229.3	228.8	93.0
	307.7	308.0	306.8	307.9	130.4
Unique reflections	41292 (4013)	52965 (5008)	34679 (3378)	49771 (4812)	31458 (3075)
Completeness (%)	99.7 (98.6)	99.5 (95.8)	99.7 (98.1)	99.7 (98.2)	100.0 (100.0)
Wilson B-factor	172	153	176	159	16.4
R-work	0.281 (0.363)	0.276 (0.367)	0.271 (0.347)	0.278 (0.371)	0.208 (0.349)
R-free	0.292 (0.337)	0.284 (0.393)	0.289 (0.378)	0.284 (0.346)	0.232 (0.368)
Number of non-hydrogen atoms	50244				2740
macromolecules	41052				2415
ligands	9192				5
waters	0				324
Protein residues	5214				315
RMS(bonds)	0.005	0.005	0.005	0.005	0.005
RMS(angles)	0.75	0.75	0.77	0.75	0.92
Ramachandran favored (%)	91	91	91	91	95

	Dark (S$_1$)	2-flash (2F)	3-flash + 250µs (3F′)	3-flash + 500ms (3F)	thermolysin
Ramachandran outliers (%)	1.2	1.2	1.1	1.2	0
Clashscore	9.43	9.45	9.50	9.34	1.72
Average B-factor	207	174	208	180	19.6

Statistics for the highest-resolution shell are shown in parentheses. All unit cell angles are 90° for PS II structures, and α=β=90°, γ=120° for thermolysin.